Corrosion Science 166 (2020) 108444

Contents lists available at ScienceDirect

Corrosion Science

journal homepage: www.elsevier.com/locate/corsci

Improved corrosion response of squeeze-cast SiC nanoparticles reinforced AZ91-2.0Ca-0.3Sb alloy

Sourav Ganguly[a], A.K. Mondal[b,*], Smarajit Sarkar[a], A. Basu[a], S. Kumar[c], Carsten Blawert[d]

[a] Department of Metallurgical and Materials Engineering, National Institute of Technology, Rourkela, 769008, India
[b] Department of Metallurgical Engineering, Indian Institute of Technology (BHU) Varanasi, Varanasi, 221005, India
[c] Department of Metallurgical Engineering, Indian Institute of Science, Bangalore, 560012, India
[d] Magnesium Innovation Centre - MagIC, Institute of Materials Research, Helmholtz-Zentrum Geesthacht, Max-Planck Str. 1, Geesthacht, 21502, Germany

ARTICLE INFO

Keywords:
AZ91 magnesium alloy
Nanocomposite
Volta potential
Hydrogen evolution
Potentiodynamic polarization scan
Surface topography

ABSTRACT

The present work investigates the effect of SiC nanoparticle additions on corrosion response of the squeeze-cast AZ91 + 2.0Ca + 0.3Sb (wt.%) alloy subjected to immersion, hydrogen evolution, and potentiodynamic polarization scan in a 0.1 M NaCl solution. All the AZ91 + 2.0Ca + 0.3Sb + xSiC_{np} (x = 0.5, 1.0, 2.0 (wt.%)) nanocomposites demonstrate a superior corrosion resistance than the alloy, and the nanocomposite reinforced with 2.0SiC_{np} exhibits the highest corrosion resistance. The improved corrosion performance of the nanocomposites is attributed to the decrease in the potential difference between α-Mg and β-$Mg_{17}Al_{12}$ phases, reduced quantity of β-$Mg_{17}Al_{12}$ phase, and an increased amount of Al_2Ca phase following SiC nanoparticles additions.

1. Introduction

Magnesium (Mg) alloys with low density, high specific strength, and excellent damping capability have the potential to effectively substitute the existing structural materials such as aluminum and steel [1]. Thus, they became attractive to the automotive industries. However, the poor corrosion resistance of Mg alloys is a serious issue, and therefore, their widespread application is still a big challenge [2]. The most commercially used Mg-Al-based alloy is the AZ91 alloy because it possesses an exceptional combination of ambient temperature mechanical properties and resistance to corrosion [3]. Nevertheless, the AZ91 alloy has poor mechanical properties (beyond 403 K), which makes it obsolete for powertrain applications in the temperature range of 423–573 K [4]. The β-$Mg_{17}Al_{12}$ phase in the AZ91 alloy significantly governs its mechanical as well as corrosion response [4,5]. To improve the elevated temperature mechanical properties of the AZ91 alloy numerous attempts have been made to modify the microstructure of the AZ91 alloy by introducing thermally stable intermetallic via alloying additions like antimony (Sb), bismuth (Bi), calcium (Ca), silicon (Si), strontium (Sr), lead (Pb), rare earths (REs) and so on. These elements suppress the β-$Mg_{17}Al_{12}$ phase formation in the AZ91 alloy [6,7]. Further, the corrosion behavior of the AZ91 alloy is highly sensitive to its microstructure, hence the presence of intermetallic phases because of the alloying additions might play a role in increasing or decreasing its corrosion resistance [8–10]. However, the application of the modified AZ91 alloys is also limited as the improvement in creep behavior is not satisfactory. Therefore, there is a need for the development of Mg alloy-based composites.

Mg alloys-based metal matrix composites in the past few decades gained attention from various engineering sectors because of their enhanced modulus, high strength, superior wear resistance, and improved creep resistance [11]. Even so, the improvement in the mechanical properties of Mg composites comes at the expense of their corrosion resistance [12]. Chan et al. [13] observed that integrating Al_2O_3 short fibers in the AZ91 alloy reduced the corrosion resistance of the alloy in alkaline medium consisting of chloride ions. Tiwari et al. [14] observed a larger rate of corrosion in Mg-SiC composites compared to pure Mg in 1.0 M NaCl solution. The incorporation of SiC microparticles into an AZ92 alloy reduced the corrosion resistance of the composites in 3.5 wt. % NaCl solution, as reported by Pardo et al. [15]. Esmaily et al. [16] examined the corrosion response of rheo-cast AZ91-SiC_p composites and reported that the composites showed less corrosion resistance than the AZ91 alloy. Several other researchers too reported that the addition of SiC microparticles exhibited a negative effect on the corrosion response of the AZ91 alloy [17–22]. The addition of SiC, Al_2O_3, AlN, B_4C, and Y_2O_3 ceramic nanoparticles to the Mg alloys exhibited superior mechanical properties compared to the micron-sized particle reinforced composites [23]. Kukreja et al. [24] investigated the corrosion response of an AZ31 alloy and AZ31-1.5 vol.% Al_2O_3 nanocomposite. They reported that the nanocomposite exhibited better corrosion resistance

* Corresponding author.
E-mail address: akmondal.met@iitbhu.ac.in (A.K. Mondal).

https://doi.org/10.1016/j.corsci.2020.108444
Received 23 September 2019; Received in revised form 3 January 2020; Accepted 4 January 2020
Available online 08 January 2020
0010-938X/

than the alloy. The corrosion behavior of the CNTs incorporated AZ31 alloy was inspected by Fukuda et al. [25], and they reported that the corrosion resistance of the alloy was drastically decreased due to CNTs addition. Turhan et al. [26] stated that multiwall carbon nanotubes (MWCNTs) addition into pure Mg resulted in a higher corrosion rate, which was attributed to the high cathodic activity of the MWCNTs. The corrosion response of pure Mg and AZ61 alloy with CNTs in heat treated as well as non-heat treated conditions were studied by Funatsu et al. [27]. They concluded that the AZ61-CNTs nanocomposite after heat treatment exhibited improved corrosion resistance than the non-heat treated one. The effect of graphene on corrosion response of the AZ31 and AZ61 alloys was studied by Rashad et al. [28]. They demonstrated that the presence of graphene nanoparticles in the alloy increased the rate of corrosion.

Although there are several investigations on the mechanical behavior of Mg alloys-based nanocomposites [29], the number of literature reporting corrosion behavior of Mg alloy-based nanocomposites is limited. Besides, the influence of SiC nanoparticles on the corrosion response of the AZ91 alloy with alloying additions has not been reported to date. In a recent investigation, it was reported that the incorporation of SiC nanoparticles (0.5, 1.0 and 2.0) (wt.%) into the AZ91 + 2.0Ca + 0.3Sb alloy (wt.%), improved its creep [30] and wear resistance [31], which is promising considering their targeted application in powertrain components. However, the corrosion behavior of these newly developed nanocomposites is not known, which is investigated in the present manuscript. The corrosion performance of the squeeze-cast AZ91 + 2.0Ca + 0.3Sb alloy and its AZ91 + 2.0Ca + 0.3Sb + $xSiC_{np}$ (x = 0.5, 1.0, 2.0 (wt.%)) nanocomposites were examined by immersion, hydrogen evolution, and potentiodynamic polarization tests. Prior to corrosion tests, scanning Kelvin probe force microscopy was employed to estimate the Volta potential of different phases in the alloy and nanocomposites. Further, the corroded surfaces and corrosion products were characterized by scanning electron microscopy, energy-dispersive X-ray spectroscopy, X-ray diffraction, Fourier transform infrared spectroscopy, X-ray photoelectron spectroscopy, and 3D profilometry.

2. Experimental procedure

2.1. Processing of alloy and nanocomposites

The detailed procedure of synthesis of the AZ91 + 2.0Ca + 0.3Sb alloy and the AZ91 + 2.0Ca + 0.3Sb + $xSiC_{np}$ (x = 0.5, 1.0, 2.0 (wt.%)) nanocomposites has been explained in our earlier work [30], which is concisely summarized here. The AZ91 + 2.0Ca + 0.3Sb (AZXY9120) alloy with its nanocomposites having nominal compositions of AZ91 + 2.0Ca + 0.3Sb + $0.5SiC_{np}$ (NC1), AZ91 + 2.0Ca + 0.3Sb + $1.0SiC_{np}$ (NC2), and AZ91 + 2.0Ca + 0.3Sb + $2.0SiC_{np}$ (NC3) (all in wt.%) were synthesized using commercialized pure AZ91 ingots, Ca and Sb in granular form having 99% purity, and SiC nanoparticles (average size of 50 nm) and a squeeze-casting setup. The AZ91 alloy was melted at 1023 K in a non-reactive environment of Ar and SF_6 gaseous mixture. Following melting, the necessary quantity of warm Ca, Sb, and SiC nanoparticles were incorporated into the liquid metal and agitated for 5 min to homogenize the mixture. Subsequently, the melt was poured into a mold preheated at 523 K. Immediately after pouring, a pressure of 200 MPa was applied and the melt solidification took place under it. The cast ingots with 50 mm diameter and 220 mm length were produced after solidification.

2.2. Volta potential measurements

A scanning Kelvin probe force microscopy (SKPFM) (Model: Asylum research oxford instruments) was employed to examine the Volta potential difference among the phases in the AZ91 + 2.0Ca + 0.3Sb alloy and AZ91 + 2.0Ca + 0.3Sb + $xSiC_{np}$ nanocomposites. It used a Ti/Ir coated (5/20 nm) Si tip having a radius of 25 ± 10 nm functioning in tapping mode with a distance of 100 nm between the tip and sample. The specimens for the Volta potential measurements were prepared following the standard metallographic technique. The specimens were initially ground with emery papers of 1000, 1200, 1500, and 2000 grit followed by cloth polishing using diamond pastes of 0.5–1.0 μm. The surfaces were then rinsed ultrasonically with ethanol. The average value of the surface roughness of the polished specimens was around 0.2 μm (200 nm). The difference in time between the final specimen preparation and the Volta potential measurement was 1 h. All the Volta potential measurements were carried out at ambient temperature and under a controlled atmosphere. The technique used to measure the data was the double passing of the tip over the surface. In the first pass, the height data was noted in tapping mode. In the second pass, the scan was along the same line in potential mode following the height contour that was noted during the first pass.

2.3. Corrosion tests of the alloy and nanocomposites

The corrosion response of the AZ91 + 2.0Ca + 3.0Sb alloy and AZ91 + 2.0Ca + 0.3Sb + $xSiC_{np}$ nanocomposites was examined employing immersion, hydrogen (H_2) evolution, and potentiodynamic polarization scan. The solution used was 0.1 M NaCl, and all the corrosion tests were conducted at ambient temperature and a neutral pH of 7.0. The NaCl concentration used to accomplish the corrosion experiments was decided in accordance with the reported values in the literature [32]. For the corrosion tests, the specimen of 15 × 15 × 4 mm^3 were machined from the as-fabricated ingots of the alloy and nanocomposites. Prior to these tests, all the specimens were polished with different grades of emery papers (up to 2000 grit) followed by cleaning in ethanol. The specimens were then rinsed in deionized water and dried in air. The immersion tests were conducted for 4, 8, 24, 48, and 72 h duration. The specimens, following the immersion tests, were cleaned using a chromate solution (200 g/l CrO_3 + 10 g/l $AgNO_3$) in compliance with ASTM G1-03 standard and then the difference in weight was measured. The weight-loss values obtained from the immersion tests were converted to the corrosion rates using the following equation [33]:

$$CR_{IM} = 8.76 \times 10^4 \times \frac{w}{TD} \quad (1)$$

where CR_{IM} stands for the corrosion rate (mm/y) in immersion, w stands for the weight-loss per square centimeter (mg/cm^2), T signifies the time of exposure (h), and D represents the density of the alloy and nanocomposite specimens.

The hydrogen evolution tests were conducted according to the setup proposed by Song et al. [34]. The hydrogen evolution tests were performed for a duration of 10 h with readings taken after an interval of 1 h. The corrosion rate from the volume of hydrogen evolution method was calculated by using the following equation [35]:

$$CR_{HE} = 8.76 \times 10^4 \times \frac{1.085V_H}{TD} \quad (2)$$

where CR_{HE} is the corrosion rate (mm/y) in the hydrogen evolution test, V_H is the volume of hydrogen evolved per unit area (ml/cm^2).

The electrochemical experiments were executed using a potentiostat (Model: VersaStat 2263, Ametek, USA) attached to a computer. The potentiostat was attached to a three-electrode flat cell of 300 ml capacity containing a platinum (Pt) counter electrode, a silver-silver chloride electrode (Ag/AgCl) (3 mol/1 KCl, +222 mV vs standard hydrogen electrode) acted as a reference electrode, and the working electrode was the test specimen. All the potentials mentioned in the present work were referred with respect to the Ag/AgCl electrode. The specimens for the potentiodynamic polarization tests were exposed to 1.0 cm^2 surface area. Initially, each of the specimens was kept for 30 min in the solution until a stable potential was achieved, which is

denoted as the open circuit potential (OCP). Following OCP, the potentiodynamic polarization scan was performed from ± 250 mV relative to OCP at a sweep rate of 12 mV/min as per the ASTM standard.

2.4. Post corrosion characterization

The AZ91 + 2.0Ca + 0.3Sb alloy and AZ91 + 2.0Ca + 0.3Sb + $xSiC_{np}$ nanocomposites after electrochemical corrosion test with corrosion products were cleaned in deionized water and air-dried. A scanning electron microscopy (SEM) (Model: JEOL JSM 6480 L V) with energy-dispersive X-ray spectroscopy (EDS) (Model: OXFORD INCA X-ACT) attached to it was used to observe the corrosion products. X-ray diffractometer (XRD) (Model: PANalytical) with CuKα radiation (λ = 1.5418 Å) with a scanning rate of 2°/min and in the scan range of 10–80° and step size of 0.03 was used to estimate the phases present in the corrosion film. The corroded films were further examined by a Fourier transform infrared spectroscopy (FTIR) in attenuated total reflectance (ATR) mode (Model: Bruker Alpha Platinum ATR). The spectra were recorded in the infrared (IR) region of 4000–400 cm^{-1}. X-ray photoelectron spectroscopy (XPS) (Model: PHI 5000 Versa Prob II, FEI Inc.) was employed to do the qualitative analysis of the corrosion film. An Al Kα monochromatic source (hυ = 1486.6 eV) was used, and an initial survey spectrum (0 − 1200 eV) was acquired with the analyzer having passing energy of 280 eV for the qualitative and the quantitative analysis. High-resolution spectra of 20 eV were taken for appropriate elemental characterization for the following core elements Mg (2p), O (1 s), and C (1 s). The X-ray source had a beam size of 100 μm and a 45° take-off angle in regards to the surface.

The corrosion film was removed from the surface of the alloy and nanocomposite specimens by dipping them in a chromate solution (200 g/l CrO_3 + 10 g/l $AgNO_3$) as per ASTM G1-03 standard. Furthermore, the specimens were washed in deionized water and then air-dried. 3D optical profilometry (Model: Bruker Contour GT) was performed to examine the overall surface features of the alloy and nanocomposites after the cleaning of corrosion products. A field emission scanning electron microscopy (FESEM) (Model: NOVA NANOSEM 450) with energy-dispersive X-ray spectroscopy (EDS) (Model: BRUKER 127 eV) attached to it was used to observe the microstructural variations after corrosion as well as elemental mapping was carried out to observe the distribution of major elements in the corroded microstructure.

3. Results and discussion

3.1. Microstructural observation of the alloy and nanocomposites before corrosion

The microstructures of the squeeze-cast AZ91 + 2.0Ca + 0.3Sb (AZXY9120) alloy and its three AZ91 + 2.0Ca + 0.3Sb + $xSiC_{np}$ nanocomposites were discussed in our preceding work [30] and are briefly presented here. Fig. 1(a–d) presents the SEM micrographs of the alloy and nanocomposites before the corrosion test. In the AZXY9120 alloy, the α-Mg (primary Mg) phase, β-$Mg_{17}Al_{12}$ phase along with the skeleton-shaped Al_2Ca phase, were present. All these phases also existed in each of the nanocomposites. As the content of SiC nanoparticles increased in the alloy, the fraction of the β-$Mg_{17}Al_{12}$ phase decreased. The volume fractions of the β-$Mg_{17}Al_{12}$ phase calculated using the ImageJ software were 9.45 ± 0.32, 8.18 ± 0.21, 6.78 ± 0.27, and 5.43 ± 0.18 % in the AZXY9120, NC1, NC2, and NC3, respectively. The lowest percentage of the β-$Mg_{17}Al_{12}$ phase was detected in the NC3 nanocomposite. The addition of SiC nanoparticles provided large numbers of sites for heterogeneous nucleation of the α-Mg phase. In the present investigation, the α-Mg phase is a solid solution of Al, Ca and other elements in Mg. Since the numbers of nucleation of the α-Mg phase were more following the additions of SiC nanoparticles, a greater amount of Al went into the solid solution. Accordingly, the amount of Al available for Mg to form the β-$Mg_{17}Al_{12}$ phase reduced, resulting in the overall decrease of the volume fraction of the β-$Mg_{17}Al_{12}$ phase in all the nanocomposites. Nie et al. [36] in their investigation too reported that with the addition of SiC nanoparticles into the AZ91 alloy, the volume fraction of the β-$Mg_{17}Al_{12}$ phase reduced considerably. As the content of SiC nanoparticles in the alloy was increased, the fraction of the Al_2Ca phase also increased, and the values were 4.49 ± 0.19, 5.34 ± 0.24, 6.38 ± 0.27, and 7.81 ± 0.12 % in the AZXY9120, NC1, NC2, and NC3, respectively. The maximum content of the Al_2Ca phase was in the NC3 nanocomposite.

Fig. 2(a) shows the bright field and Fig. 2(b) is the corresponding dark field TEM micrographs of the squeeze-cast NC3 nanocomposite exhibiting the distribution of the SiC nanoparticles in the AZXY9120 alloy matrix. Fig. 2(c) represents the SAD pattern corresponding to (a), and Fig. 2(d) shows the bright field TEM micrograph showing the interface of the SiC nanoparticles and the AZXY9120 alloy matrix. The SiC nanoparticles were mainly distributed in the α-Mg matrix with negligible agglomeration. The detailed description of the TEM images showing the distribution of the nanoparticles was reported in our previous work [30].

3.2. Analysis of Volta potential

Fig. 3(a & b) shows the surface topography and Volta potential map obtained from the AZXY9120 alloy with the corresponding Volta potential profiles. The base of the profile corresponding to the α-Mg matrix was considered as the reference. The values of Volta potential referred here were measured relative to the α-Mg matrix. The Volta potential profile corresponding to line 1 in Fig. 3(b) illustrates the presence of two peaks, one at a lower potential and the other at a higher potential in comparison to the α-Mg matrix. The peak at higher potential is corresponding to the β-$Mg_{17}Al_{12}$ phase, and it has a potential of 1200 ± 50 mV. On the other hand, the peak at a lower potential corresponds to the Al_2Ca phase, and it has a potential of 610 ± 36 mV. The Volta potential profile corresponding to line 2 in Fig. 3(b) depicts the presence of a single peak referring to the β-$Mg_{17}Al_{12}$ phase with a potential of 985 ± 42 mV. Blucher et al. [37] studied the role of the β-$Mg_{17}Al_{12}$ phase on the atmospheric corrosion behavior of the AZ91 alloy using SKPFM and reported that the Volta potential of the β-$Mg_{17}Al_{12}$ phase was higher than the α-Mg. Mingo et al. [38] added Mn, Nd, Y, Ca, and Sn as the minor elements into the Mg-9Al alloy. They reported higher Volta potentials of the secondary precipitates formed following the additions compared to the base alloy. In addition, they reported that the Ca-rich phase had a lower potential than the β-$Mg_{17}Al_{12}$ phase. Fig. 3(c & d) shows the surface topography and the Volta potential map with the corresponding Volta potential profiles obtained from the NC3 nanocomposite as a representative for the nanocomposites. The Volta potential profile from line 1 in Fig. 3(d) illustrates the presence of two peaks similar to those observed in the alloy. The peak at the higher potential was corresponding to the β-$Mg_{17}Al_{12}$ phase with a potential of 1030 ± 55 mV, whereas the peak at a lower potential was corresponding to the Al_2Ca phase with a potential of 560 ± 30 mV. The Volta potential profile from line 2 in Fig. 3(d) depicts the presence of a single peak referring to the β-$Mg_{17}Al_{12}$ phase with a potential of 870 ± 44 mV. The Volta potential of the β-$Mg_{17}Al_{12}$ phase was higher in the alloy and it was lower in the NC3 nanocomposite. The reductions in Volta potential in the NC3 nanocomposite compared to the alloy were 14.2% for line 1 and 11.6% for line 2 of the Volta potential profiles. Thus, the Volta potential of the β-$Mg_{17}Al_{12}$ phase was more cathodic than that of the Al_2Ca phase. Further, the Volta potential of the Al_2Ca phase in the alloy (i.e., 610 mV) was higher than that observed in the NC3 nanocomposite (i.e., 560 mV). Thus, the incorporation of SiC nanoparticles in the alloy reduced the Volta potential of both the β-$Mg_{17}Al_{12}$ and Al_2Ca phases. The influences of alloying elements and nanoparticles additions on the Volta potential of the Mg-Al alloys have been reported in the literature [25,27,39–42].

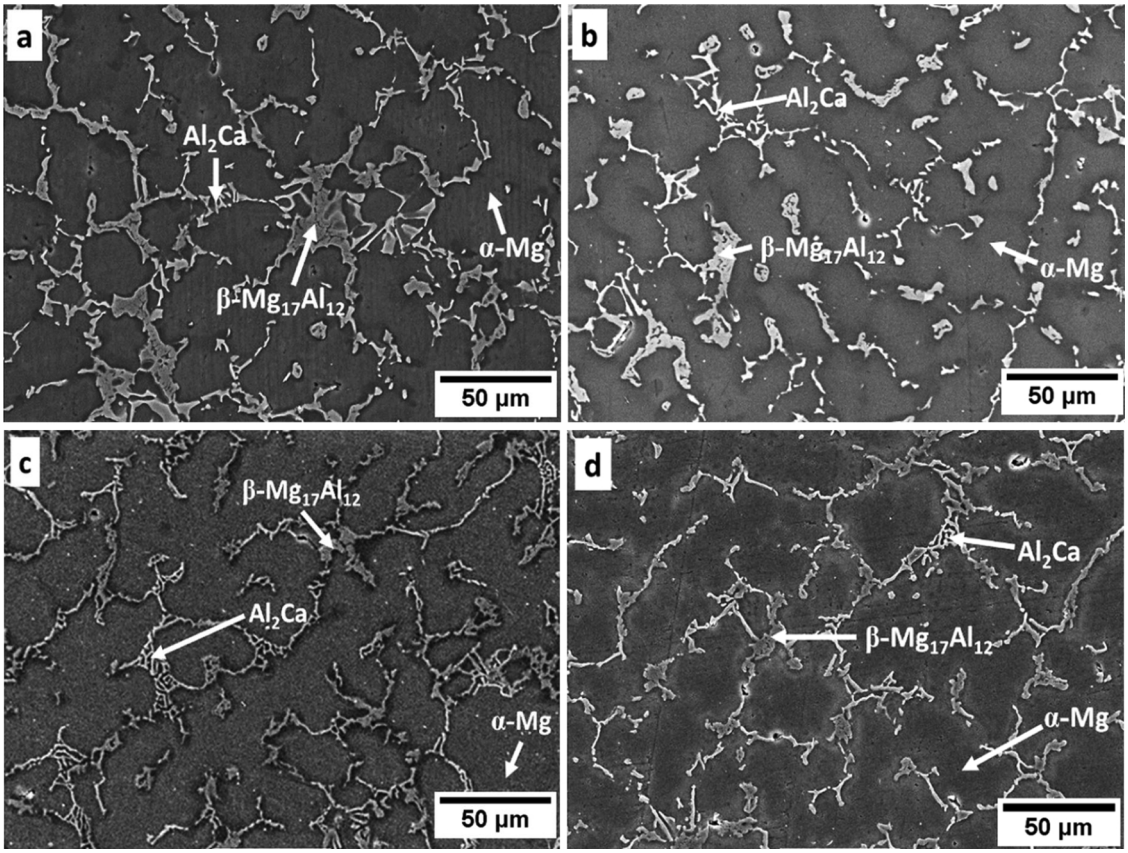

Fig. 1. SEM micrographs of the (a) AZXY9120 alloy; (b) NC1, (c) NC2, and (d) NC3 nanocomposites [Reprinted with permission from Ref. [30].

Örnek et al. [42] concluded the increase in Volta potential of a less noble matrix following the addition of a more noble element in it. The SiC nanoparticles employed in the present investigation were nobler than the α-Mg phase. Therefore, the increase in the Volta potential of the α-Mg phase was due to the dispersion of noble SiC nanoparticles. The SiC nanoparticles were mainly distributed in the α-Mg matrix with negligible agglomeration as shown in Fig. 2. Accordingly, a less intense micro-galvanic corrosion between the α-Mg and the β-$Mg_{17}Al_{12}$ phases was expected to take place in the nanocomposites as compared to the alloy. The Volta potential measurements of the NC1 and NC2 nanocomposites too exhibited similar behavior as the NC3 nanocomposite, i.e., the reduction in the Volta potential of both the β-$Mg_{17}Al_{12}$ and Al_2Ca phases compared to that of the alloy. However, the reduction in Volta potential was the maximum in the NC3 nanocomposite.

3.3. Evaluation of corrosion rate

3.3.1. Immersion test

Fig. 4(a) shows the variation of weight-loss per unit surface area of the AZXY9120 alloy and AZXY9120 + xSiC_{np} nanocomposites. The plot demonstrated that the weight-loss of both the alloy and nanocomposites increased with an increase in immersion time, as expected and it was more in the former than the later for all test duration. Among the nanocomposites, the NC3 revealed the lowest weight-loss for all test duration. The reductions in weight-loss values of the NC3 nanocomposite compared to the alloy were 64, 51, 51, 53 and 41% after 4, 8, 24, 48 and 72 h, respectively. Fig. 4(b) depicts the corrosion rate (mm/y) calculated from the weight-loss using Eq. 1 as a function of the SiC nanoparticles content. All the nanocomposites revealed a lower corrosion rate than the alloy. Among the nanocomposites, the lowest corrosion rate was revealed by the NC3 nanocomposite for all test duration. Thus, the immersion test results confirmed that the addition of SiC nanoparticles to the AZXY9120 alloy substantially improved its corrosion resistance.

3.3.2. Hydrogen evolution

The predominant corrosion reaction of Mg in aqueous medium is depicted by the following reaction [43]:

$$Mg + 2H_2O = Mg^{2+} + 2OH^- + H_2 \quad (3)$$

The reaction indicates that one Mg atom yields one hydrogen gas molecule (H_2). Thus, quantifying the volume of evolved hydrogen gas is directly correlated with the weight-loss of the dissolved Mg [43,44]. Fig. 5(a) illustrates the variation of volume of hydrogen gas evolved per unit surface area as a function of elapsed time for the AZXY9120 alloy and AZXY9120 + xSiC_{np} nanocomposites. The incorporation of SiC nanoparticles in the alloy reduced the hydrogen gas evolution in all the nanocomposites in contrast to the alloy. The evolution of hydrogen gas after an initial period increased with an increase in the exposure time in both the alloy and nanocomposites. Three stages of hydrogen evolution were observed, and these are marked in the plots. The stage I is corresponding to an initial low hydrogen evolution; stage II presents a gradual increase in the hydrogen evolution, and stage III revealed a steady acceleration in the hydrogen evolution. The three stages were distinct in the nanocomposites, whereas the first and the second stages were combined in case of the alloy. In the alloy, owing to the large Volta potential difference between the α-Mg and the β-$Mg_{17}Al_{12}$ phases and poor barrier provided by the β-$Mg_{17}Al_{12}$ phase, the α-Mg phase dissolved faster and accordingly, a higher rate of hydrogen evolution took place after an initial incubation period. In contrast, owing to the small Volta potential difference between the α-Mg and the β-$Mg_{17}Al_{12}$ phases, the presence of a reduced amount of the β-$Mg_{17}Al_{12}$ phase, and the higher amount of the Al_2Ca phase, the dissolution of the α-Mg phase was lower in the nanocomposites compared to the alloy. Consequently,

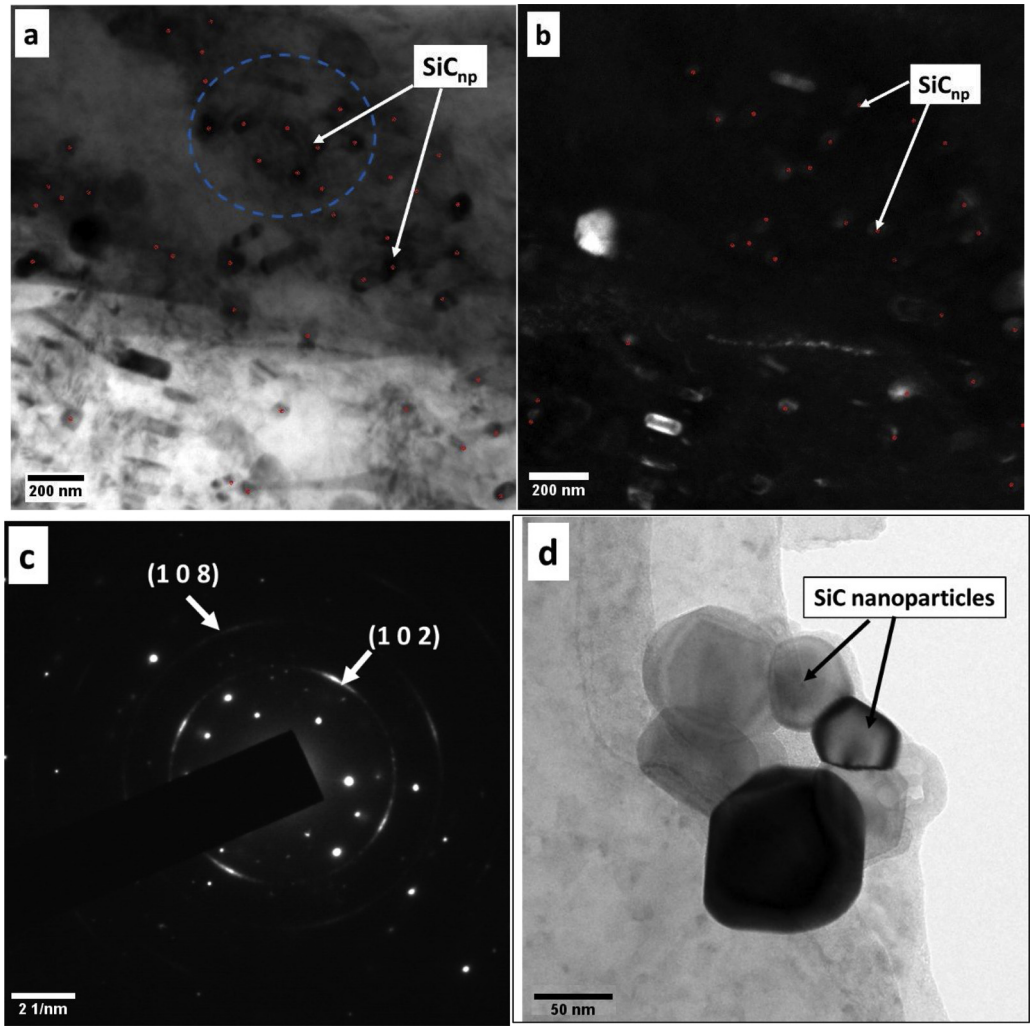

Fig. 2. (a) Bright field and (b) corresponding dark field TEM micrographs of the as-cast NC3 nanocomposite exhibiting the distribution of the SiC nanoparticles in the alloy matrix, (c) SAD pattern corresponding to (a), and (d) Bright field TEM micrograph showing the interface of the SiC nanoparticles and the alloy matrix [Reprinted with permission from Ref. [30].

the rate of hydrogen evolution in the nanocomposites was substantially lower than that in the alloy. Among the nanocomposites, the NC3 exhibited the lowest hydrogen evolution, and it was 23% lower than the alloy for the total duration. The corrosion rates (mm/y) were calculated from the volume of hydrogen evolved, employing Eq. 2 for the alloy and nanocomposites, and the results are shown in Fig. 5(b) as a function of elapsed time. All the nanocomposites displayed a reduced corrosion rate in contrast to the alloy, and it was the lowest in the NC3.

3.3.3. Electrochemical corrosion response

3.3.3.1. Open circuit potential. The variation of open circuit potential (OCP) against time for the AZXY9120 alloy and AZXY9120 + xSiC$_{np}$ nanocomposites is shown in Fig. 6(a). The values of OCP for all the materials were almost stable from the beginning of the exposure. The slight unevenness in the potential curves was due to the attack of the surface by chloride ions (Cl^-) from the solution and its subsequent passivation by the formation of corrosion products. The mean values of OCP calculated from Fig. 6(a) for the alloy and nanocomposites are shown in Fig. 6(b). The average OCP values recorded were −1365, −1343, −1327 and −1305 mV for the AZXY9120 alloy, NC1, NC2 and NC3, respectively. Thus, the addition of SiC nanoparticles shifted the OCP of all the nanocomposites towards more noble values, and the NC3 was the noblest with an average shift of +60 mV compared to the alloy. The shifting of OCP to the more positive potential for all the nanocomposites was attributed to the ennoblement of the α-Mg phase following the additions of the SiC nanoparticles in the AZXY9120 alloy.

3.3.3.2. Potentiodynamic polarization scan. The typical curves of potentiodynamic polarization scan of the AZXY9120 alloy and AZXY9120 + xSiC$_{np}$ nanocomposites following 8 h of exposure are shown in Fig. 7, and the polarization data derived from it are provided in Table 1. It is observed that all the nanocomposites revealed higher corrosion potential (E_{corr}) than the alloy. This implies that the incorporation of SiC nanoparticles shifted the corrosion potential of all the nanocomposites towards more positive values, and the noblest E_{corr} (i.e., −1295 mV) was observed in the NC3 nanocomposite. The increase in corrosion potential of the nanocomposite was attributed to the distribution of noble SiC nanoparticles, which raised the potential towards more positive values. The corrosion current density (I_{corr}) is a parameter that assesses a material's resistance to any corrosion reaction. In the present investigation, the incorporation of SiC nanoparticles in the alloy decreased the values of corrosion current density (I_{corr}). Thus, all the nanocomposites exhibited significantly lower I_{corr} values than the alloy, as shown in Table 1. The NC3 revealed the lowest I_{corr} value of 2.92 μA/cm^{2,} and it was 82% lower than that of the alloy (15.87 μA/cm^2). A higher value of the corrosion current density in the alloy implied an increased corrosion rate, while a lower corrosion current

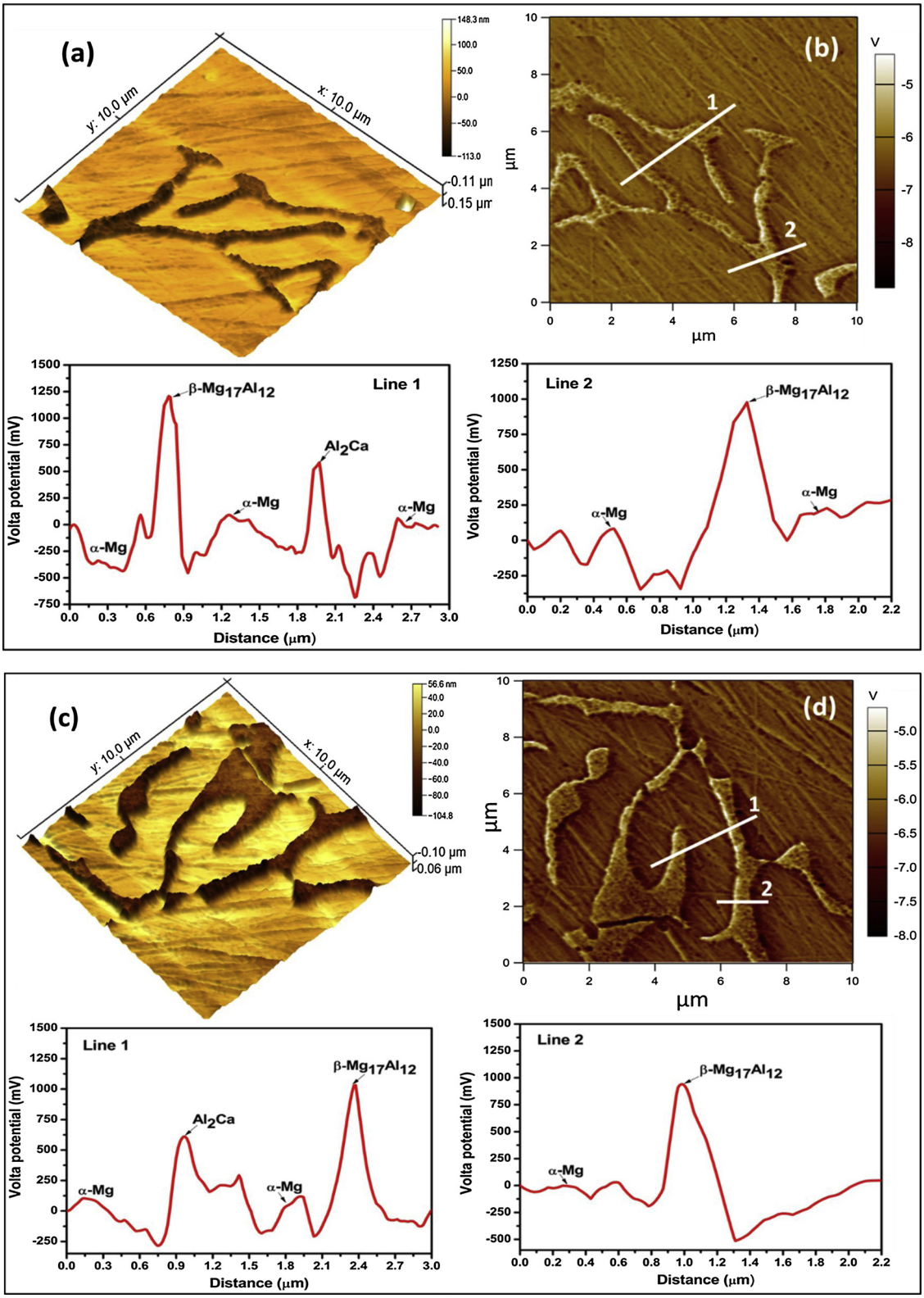

Fig. 3. The surface topographies, Volta potential maps, and the corresponding potential profiles of the AZXY9120 alloy (a, b); and NC3 nanocomposite (c, d) obtained before the corrosion tests.

density values in the nanocomposites indicated a slower rate of corrosion. The incorporation of SiC nanoparticles lowered the Volta potential difference between the α-Mg and the β-$Mg_{17}Al_{12}$ phases (as observed in the SKPFM results), reduced the amount of β-$Mg_{17}Al_{12}$ phase, and increased the amount of the Al_2Ca phase (as observed in as-cast microstructure). Accordingly, the dissolution of the α-Mg phase in the nanocomposites was lowered that decreased the amount of charge transfer and resulted in the reduction of corrosion current density. The detailed contribution of microstructures on the corrosion response of the alloy and nanocomposites have been analyzed further and

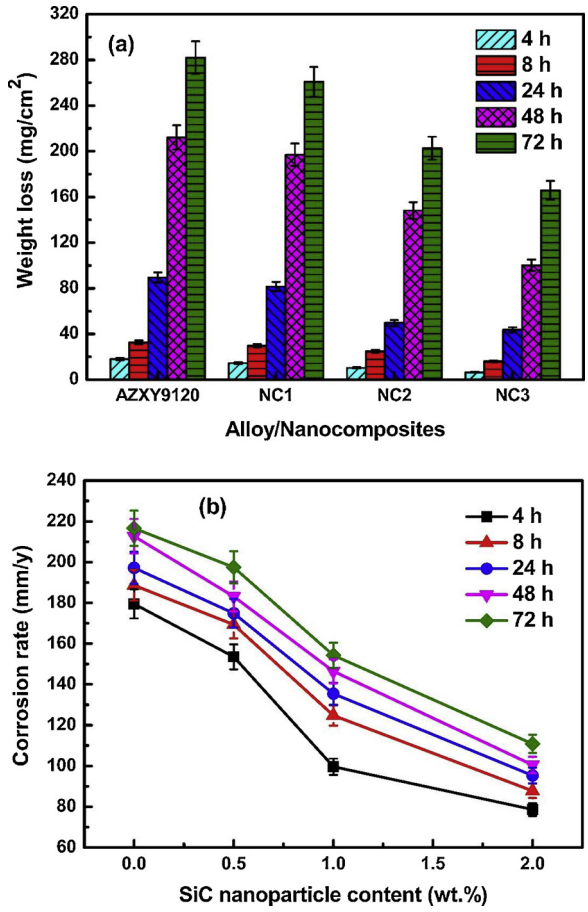

Fig. 4. (a) Weight-loss measured following immersion tests for different time intervals, and (b) the variation of corrosion rate calculated from (a) as a function of SiC nanoparticles content for the AZXY9120 alloy and nanocomposites.

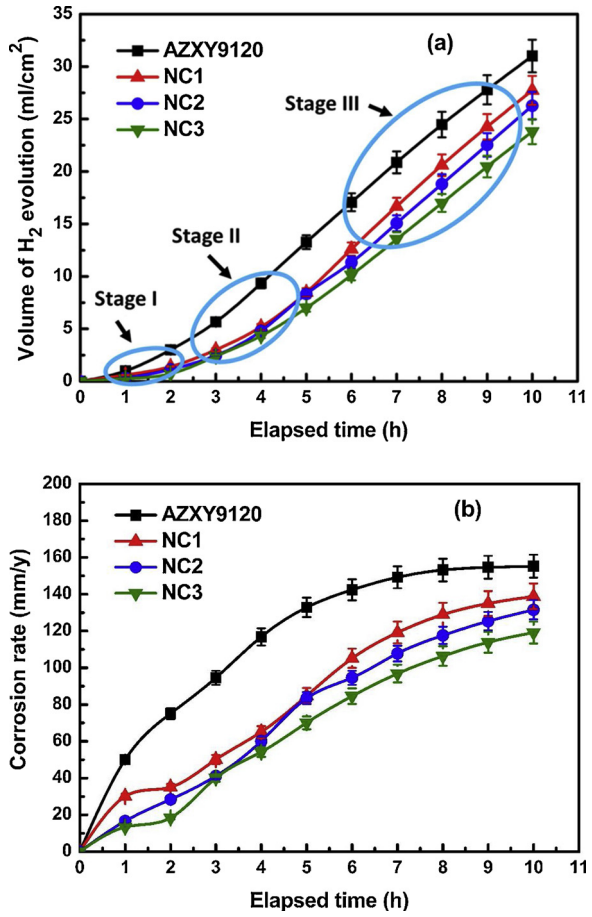

Fig. 5. The variation of (a) volume of hydrogen evolved, and (b) the corrosion rate determined from (a) as a function of elapsed time for the AZXY9120 alloy and nanocomposites.

explained in Section 3.5.2. Kukreja et al. [24] in their investigated too reported that with the addition of Al_2O_3 nanoparticles in the AZ31 alloy, the corrosion potential shifted towards positive values and the corrosion current density reduced significantly. The reported values of the corrosion rates of the AZ91 alloy reinforced with SiC micro particles and produced by different techniques have been compared with that of the nanocomposites employed in the present investigation in Table 2. The squeeze-cast nanocomposites in the present investigation exhibited the superior corrosion resistance compared to the AZ91-based microcomposites produced by squeeze-cast (SC) or semi-solid casting (SSC) techniques. Several researchers reported that the addition of SiC microparticles exhibited a negative effect on the corrosion response of the Mg alloys [14,17,18]. However, the results of the SiC nanoparticles reinforced AZXY9120 alloy in the present investigation exhibited an improved corrosion response of the alloy, which is beneficial for the development of the Mg alloy-based nanocomposites.

3.4. Characterization of corrosion products

3.4.1. SEM observation

Fig. 8(a–d) illustrates the SEM micrographs of corrosion films of the electrochemical corrosion tested AZXY9120 alloy and AZXY9120 + x-SiC_{np} nanocomposites. The surface of the alloy, as shown in Fig. 8(a) was completely covered with non-uniform corrosion products. A large number of discontinuous deep cracks covering a major area of the alloy surface were observed, which suggests the poor stability of the corrosion film. On the contrary, the morphology of the corrosion film observed on the surface of the nanocomposites was slightly different, as shown in Fig. 8(b–d). With an increase in SiC nanoparticles content in the nanocomposites, the cracks gradually became shallow and their number reduced. Among the nanocomposites, the NC3 displayed the lowest numbers of shallow cracks with little discontinuities, as shown in Fig. 8(d). These shallow cracks were less connected to each other, suggesting relatively more stable corrosion products.

3.4.2. XRD and FTIR analysis

Fig. 9(a) illustrates the XRD peaks acquired from the electrochemical corrosion tested AZXY9120 alloy and AZXY9120 + xSiC_{np} nanocomposites with corrosion products on them. It is noticeable from the figure that peaks corresponding to $Mg(OH)_2$ were detected along with the peaks of α-Mg, β-$Mg_{17}Al_{12}$, and Al_2Ca phases in both the alloy and nanocomposites. Nonetheless, the peak intensity of $Mg(OH)_2$ was the highest in the alloy and the lowest in the NC3 nanocomposite. Thus, the amount of $Mg(OH)_2$ phase in the corrosion product of the nanocomposites reduced with an increase in the SiC nanoparticles additions. Since the corrosion experiments were conducted in an open atmosphere, the involvement of CO_2 in the Mg corrosion reactions cannot be neglected. The CO_2 from atmosphere forms carbonates and hydrated carbonates reacting with $Mg(OH)_2$, as per the following reactions [43,45]:

$$Mg(OH)_2 + CO_2 \rightarrow MgCO_3 + H_2O \quad (4)$$

$$MgCO_3 + 3H_2O \rightarrow MgCO_3.3H_2O \quad (5)$$

$$5MgCO_3.3H_2O \rightarrow 4MgCO_3.Mg(OH)_2.4H_2O + CO_2 + 10H_2O \quad (6)$$

Nonetheless, the crystalline structure of magnesium carbonate ($MgCO_3$)

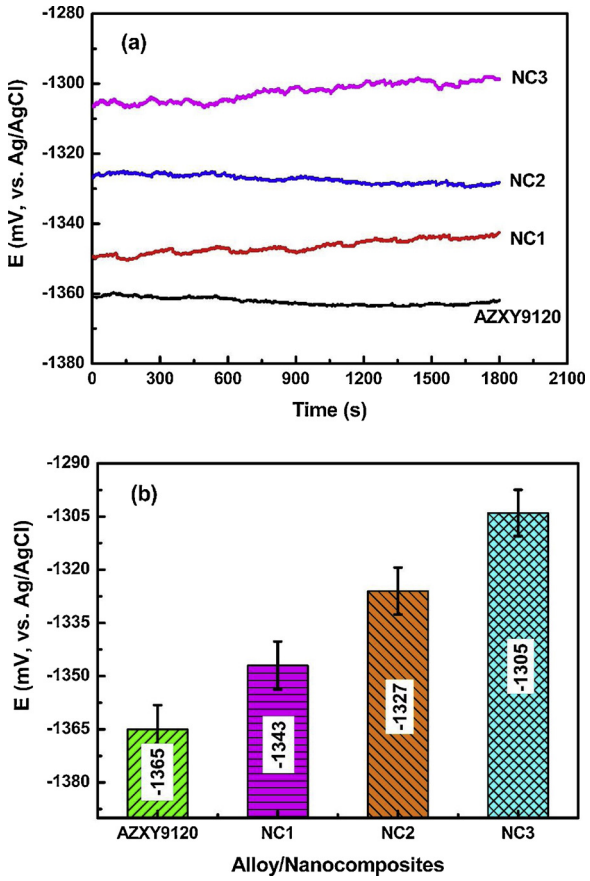

Fig. 6. The variation of (a) open circuit potential (OCP) with elapsed time, and (b) average values of the OCP determined from (a) for the AZXY9120 alloy and nanocomposites.

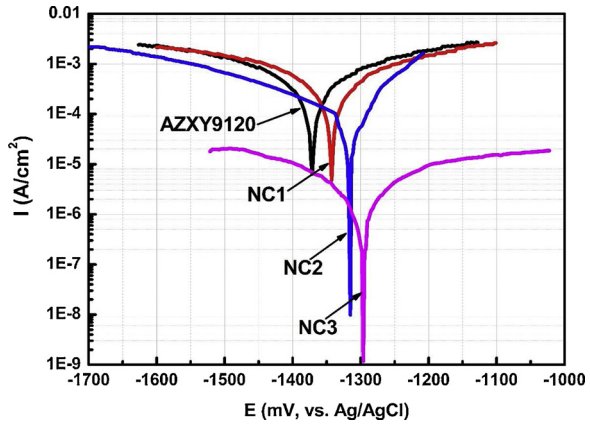

Fig. 7. Potentiodynamic polarization curves for the AZXY9120 alloy and nanocomposites.

Table 1
Summary of the various parameters calculated from the potentiodynamic polarization curves.

Alloy/ Nanocomposite	E_{corr} (mV)	I_{corr} (μA/cm^2)	β_a (mV)	β_c (mV)
AZXY9120	−1370 ± 6	15.9 ± 0.7	320 ± 9.7	−428 ± 5.6
NC1	−1348 ± 9	13.3 ± 0.4	313 ± 7.2	−367 ± 6.9
NC2	−1325 ± 7	6.5 ± 0.6	36 ± 4.3	−243 ± 3.7
NC3	−1295 ± 10	2.9 ± 0.8	87 ± 5.7	−219 ± 3.4

is poor and difficult to identify using XRD [46]. Therefore, further analysis of the corrosion film was carried out using FTIR.

Fig. 9(b) displays the FTIR absorbance spectra of the corrosion products formed on the electrochemical corrosion tested AZXY9120 alloy and AZXY9120 + xSiC_{np} nanocomposites. It is evident that all the specimens exhibited a sharp peak at 3739 cm^{-1} and a broad spanning from 3696 to 3469 cm^{-1}. These peaks were corresponding to the $(OH)^{-1}$ stretched vibration band of brucite ($Mg(OH)_2$) and hydromagnesite ($Mg_5(CO_3)_4(OH)_2.4(H_2O)$). The H_2O peak confirming the presence of hydromagnesite is generally observed at 3440 cm^{-1}. However, it was absent in the present case. On the other hand, the presence of a small and weak CO_3^{-2} asymmetric bending peak observed at 1651 cm^{-1}, and 845 cm^{-1} in both the alloy and nanocomposites suggested that some amount of hydromagnesite might form. A sharp peak at 2360 cm^{-1} corresponding to the CO_2 stretching vibration band revealed the presence of CO_2 at the surface. The asymmetric peak of CO_3^{-2} observed at 1526 cm^{-1}, and 845 cm^{-1} in both the alloy and nanocomposites showed the clear presence of nesquehonite ($MgCO_3.3H_2O$). Thus, it was concluded from the results of FTIR that the main corrosion products formed during the corrosion process were brucite ($Mg(OH)_2$) and nesquehonite ($MgCO_3.3H_2O$) [46]. A low amount of nesquehonite was converted to hydromagnesite as the test duration was not long.

3.4.3. XPS analysis

Fig. 10(a & b) shows the high-resolution Mg 2p XPS spectra of the electrochemical corrosion tested AZXY9120 alloy and NC3 nanocomposite, respectively. The spectra disclosed individual binding energy peak at 47.8 ± 0.2 eV that was for Mg in its oxidized state of Mg^{+2}. The Mg constituent changed to a combination of $Mg(OH)_2$ peak at 47.4 ± 0.5 eV, $MgCO_3$ peak at 48.4 ± 0.3 eV and a small MgO peak at 50.0 ± 0.4 eV. The peak corresponds to metallic Mg at 49.5 ± 0.1 eV was not observed in the spectra. The high-resolution O 1s spectra shown in Fig. 10(c & d) corresponding to the alloy and NC3 nanocomposite, respectively revealed three components. For both the alloy and NC3, one intense peak at a binding energy of 529.5 ± 0.3 eV was corresponding to the presence of oxygen-containing compounds like $MgCO_3$ and $Mg(OH)_2$. In addition, two binding energy peaks with lower intensities observed at 528.5 ± 0.2 and 530.5 ± 0.5 eV were corresponding to oxygen in MgO and H_2O, respectively. Fig. 10(e & f) illustrated high-resolution C 1s spectra of the alloy and NC3, respectively. The spectra were fitted with two constituents at two binding energies, i.e., at 282.0 ± 0.2 eV corresponds to the existence of C—C/C—H groups; and the other at 287.8 ± 0.3 eV corresponding to the presence of $MgCO_3$ [47]. The formation of $MgCO_3$ was associated with the CO_2 diffusion from the surroundings and reaction of CO_2 with corrosion film [48]. The XPS analysis revealed that the $Mg(OH)_2$ and $MgCO_3$ were the main constituents of the corrosion products. The similar XPS results of corroded products formed on the surfaces of AZ-based alloys were also reported [47,48].

The carbonate-rich layer formed as a corrosion product on the surface of the Mg alloy lowers the conductivity of the electrolyte and blocks the anode or cathode, which helps in slowing down the corrosion of Mg alloy [45]. However, it is difficult to quantify the carbonates present in the corrosion products employing the FTIR or XPS as the carbonates are the by-products of corrosion reaction. The XRD results in the present investigation indicated that with the addition of SiC nanoparticles in the AZXY9120 alloy, the intensity of the $Mg(OH)_2$ peak reduced confirming the reduction of its amount. The formation of the carbonate-rich layer is directly related to the presence of $Mg(OH)_2$ on the surface. Therefore, it is expected that lower is the $Mg(OH)_2$ content, lower is the carbonates content in the corrosion product. Thus, the incorporation of the SiC nanoparticles reduced the carbonate content in the corrosion product. However, quantification is beyond the scope of the present investigation.

Table 2
Comparison of corrosion rates of the nanocomposites employed in the present investigation with the reported values of the SiC microparticles reinforced pure Mg and AZ91 alloy.

References	Matrix	Reinforcement (vol.%)	Average particle size (μm)	Processing	Environment	Corrosion rate (mg/cm^2/day)
Zhang et al. [17]	AZ91	0.0 SiC_p	10	Semi-solid casting	3.5 wt.% NaCl	1.2
		5.0 SiC_p				2.7
		10.0 SiC_p				7.5
		15.0 SiC_p				9.6
Mingo et al. [18]	AZ91	SiC_p	15-25	Semi-solid casting	3.5 wt.% NaCl	0.07
						2.0
						11.0
		2.0 SiC_p				12.0
		5.0 SiC_p				
		10.0 SiC_p				
Lopez et al. [20]	Mg	1.0 SiC_p	3	Magnetron sputtering	3.5 wt.% NaCl	0.01 (current density, mA/cm^2)
Tiwary et al. [14]	Mg	0.0 SiC_p	25	Mechanical disintegration deposition	1.0 M NaCl	6.4
						8.6
		6.0 SiC_p				21.7
		16.0 SiC_p				
Present study	AZ91 + 2.0Ca + 0.3Sb	SiC_{np}	0.05	Squeeze-casting	0.1 M NaCl	6.7
						5.6
		0.3 SiC_{np}				2.7
		0.6 SiC_{np}				1.2
		1.2 SiC_{np}				

3.5. Characterization of the corroded surface after removal of corrosion products

3.5.1. Analysis of surface topography

Fig. 11(a–d) displays the 3D surface topographic features, and surface roughness (R_a) values of the electrochemical corrosion tested AZXY9120 alloy and AZXY9120 + xSiC_{np} nanocomposites after removal of corrosion products from them. The initial surface roughness of the alloy before the corrosion test was 0.5 μm, and it varied from 0.4 to 0.5 μm for the nanocomposites. The surface roughness estimated following the corrosion test correlates with the extent of corrosion that took place on the surface [49,50]. The AZXY9120 alloy illustrated the maximum surface roughness (R_a) of 24.63 μm, as shown in Fig. 11(a). The 3D topography of the alloy displayed the presence of a large

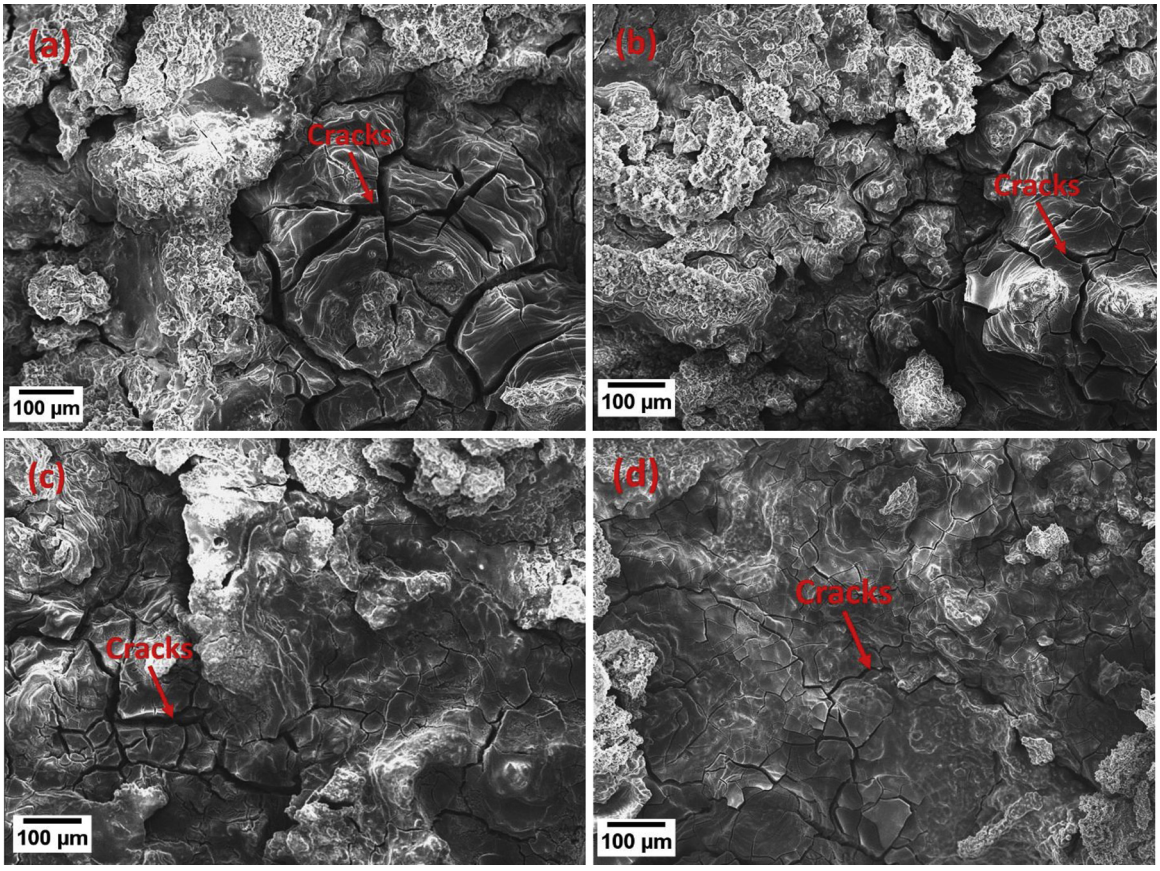

Fig. 8. SEM micrographs of the corroded surfaces with corrosion products for the (a) AZXY9120 alloy; (b) NC1, (c) NC2, and (d) NC3 nanocomposites.

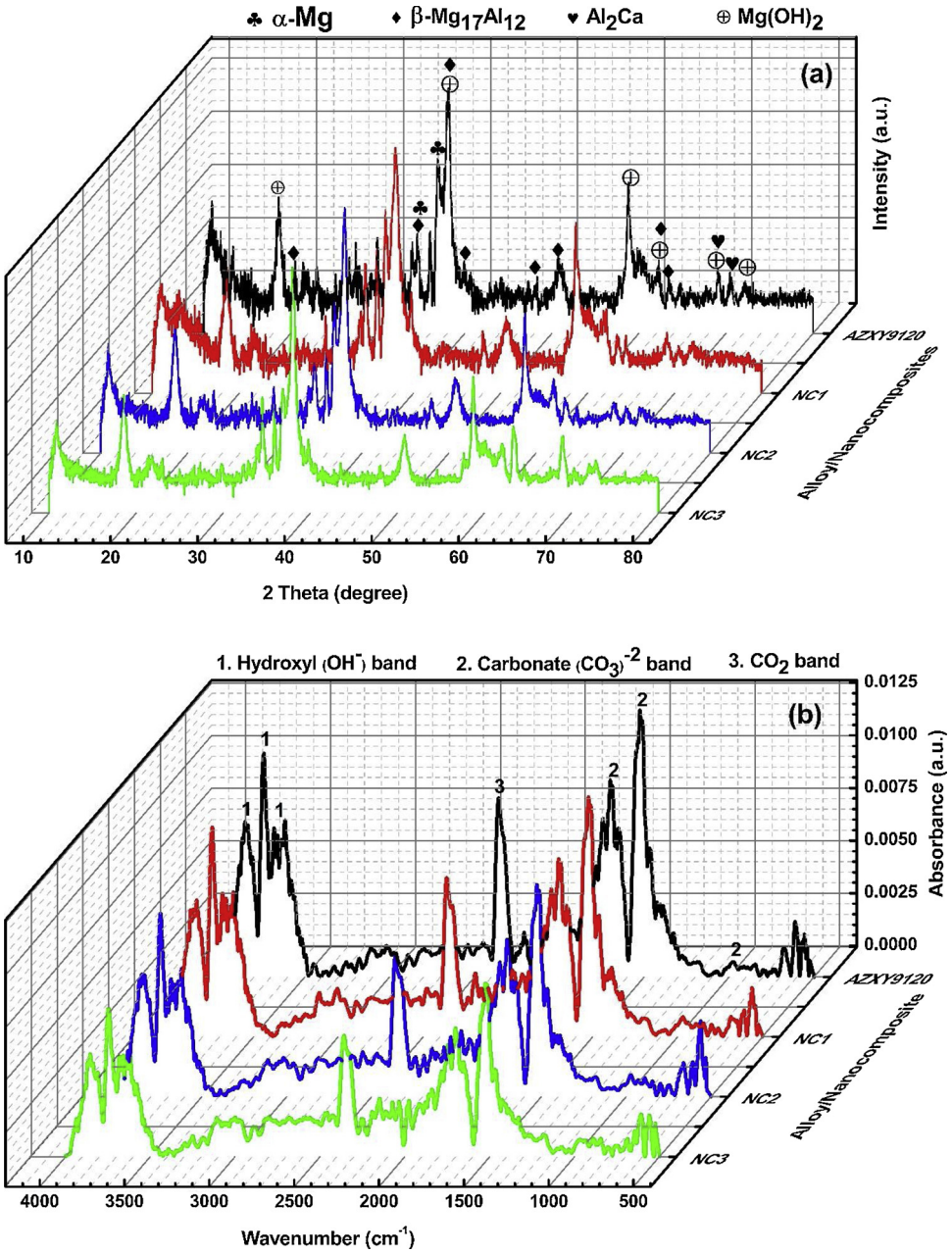

Fig. 9. (a) XRD and (b) FTIR patterns obtained from the corroded surfaces with corrosion products for the AZXY9120 alloy and nanocomposites.

number of deep valleys and peaks, which were related to the high corrosion rate of the alloy. With the incorporation of SiC nanoparticles in the alloy, the surface roughness values of all the nanocomposites decreased considerably, as observed in Fig. 11(b–d). The surface topographies of the nanocomposites demonstrated relatively shallower valleys and peaks than the alloy indicating lower corrosion rates of all the nanocomposites. Among the nanocomposites, the NC3 exhibited the lowest surface roughness (R_a) of 16.31 μm, as shown in Fig. 11(d). The R_a value of the NC3 nanocomposite was 34% lower than that of the alloy. The surface topography of the NC3 nanocomposite revealed the presence of very shallow valleys and peaks owing to its lowest corrosion rate among the materials employed.

3.5.2. Analysis of microstructure

Fig. 12(a–d) presents the corroded surfaces of the AZXY9120 alloy and AZXY9120 + xSiC_{np} nanocomposites after the removal of corrosion products from them. In order to understand the phases that were affected by corrosion, elemental mappings were taken from the corroded surfaces of the alloy and NC3 (representative for the nanocomposites), as shown in Fig. 13(a & b). It is evident from Fig. 12(a & d) and Fig. 13(a & b) that the α-Mg phase was affected the most by corrosion whereas, the β-$Mg_{17}Al_{12}$ and Al_2Ca phases were standing along grain boundaries of both the alloy and nanocomposites. The same behaviour was also observed in the NC1 and NC2 nanocomposites however, the α-Mg phase was the least affected by corrosion in the NC3. The SEM micrograph (Fig. 12(a)), as well as elemental mapping (Fig. 13(a)) of the alloy, revealed the presence of numerous localized corroded regions containing large pits and removal of grain interiors (α-Mg) adjacent to the β-$Mg_{17}Al_{12}$ phase by corrosion. On the contrary, the region adjacent to the Al_2Ca phase was relatively less corroded with the presence of small pits. Thus, the SKPFM results and corroded microstructure of the alloy confirmed that the β-$Mg_{17}Al_{12}$ phase was a lot more cathodic (i.e., 1200 mV) than the Al_2Ca phase (i.e., 610 mV) resulting in the substantial dissolution of α-Mg adjacent to the former

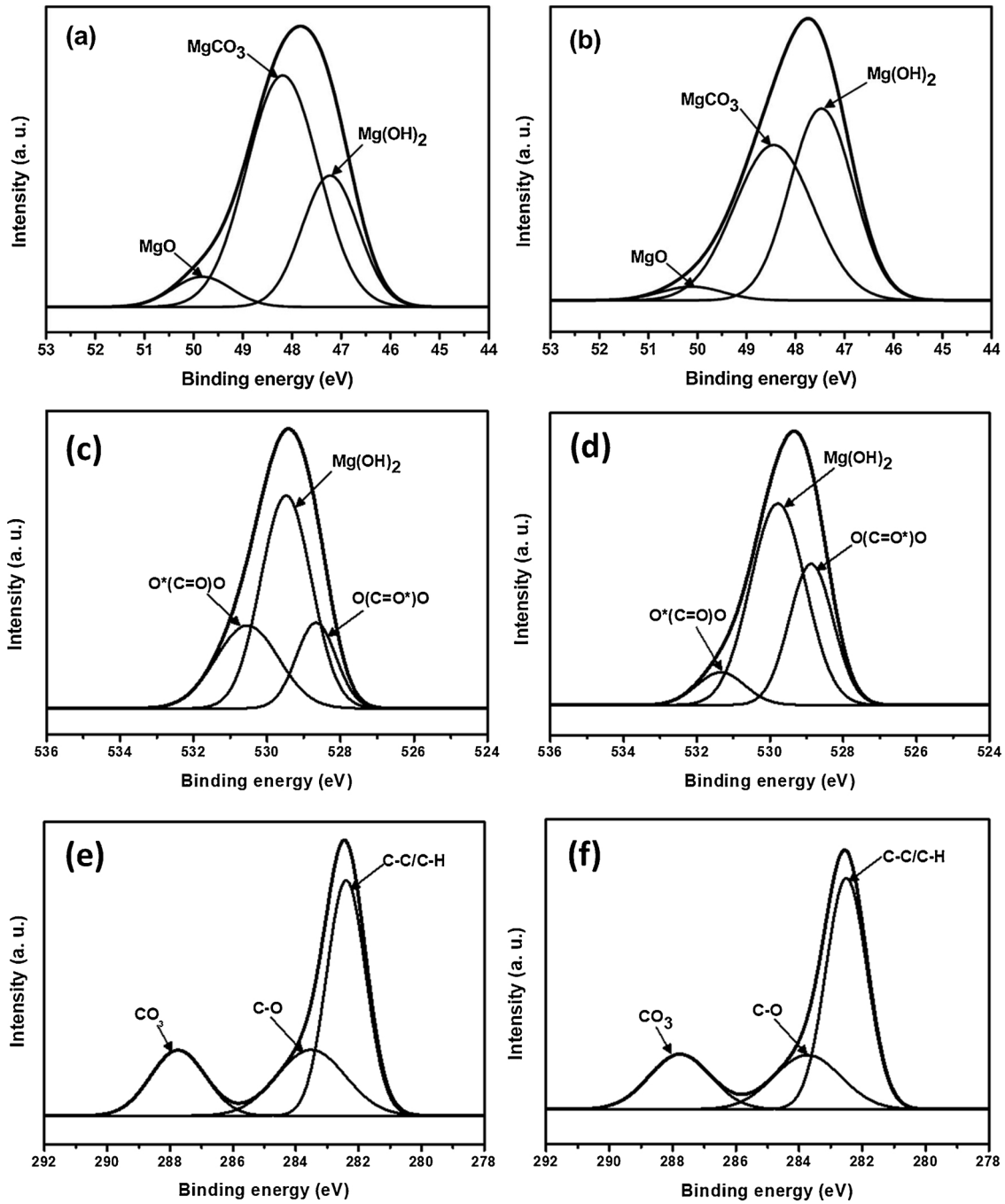

Fig. 10. High-resolution XPS spectra showing major elements Mg 2p, O 1s, and C 1s obtained from the corrosion products of the AZXY9120 alloy (a, c, e); and NC3 nanocomposite (b, d, f).

phase. The driving force for micro-galvanic corrosion between the α-Mg and β-$Mg_{17}Al_{12}$ phases was stronger than that between the α-Mg and Al_2Ca phases. Accordingly, the α-Mg phase adjacent to the β-$Mg_{17}Al_{12}$ phase was severely corroded.

As the content of SiC nanoparticles in the nanocomposites increased, the fraction of the β-$Mg_{17}Al_{12}$ phase decreased, and it was the lowest in the NC3 nanocomposite. Conversely, the fraction of the Al_2Ca phase increased with SiC nanoparticles addition, and it was the maximum in the NC3. The regions adjacent to the β-$Mg_{17}Al_{12}$ phase even in the nanocomposites were corroded. However, the extent of the corroded region decreased as its content reduced in the nanocomposites. In addition, the number of pits and regions of grain interior (α-Mg) removed by corrosion reduced significantly in all the nanocomposites, and the feature was the lowest in the NC3 nanocomposite. In the nanocomposites too, the region adjacent to the Al_2Ca phase was relatively less corroded. The addition of SiC nanoparticles suppressed the β-$Mg_{17}Al_{12}$ phase formation and increased the Al_2Ca phase in the nanocomposites, and therefore, the extent of corrosion was less in all the nanocomposites. The NC3 nanocomposite with the lowest and the highest amount of β-$Mg_{17}Al_{12}$ and Al_2Ca phases respectively exhibited the best corrosion resistance among the specimen tested.

4. Conclusions

The present work investigated the corrosion performance of the squeeze-cast AZ91 + 2.0Ca + 0.3Sb alloy reinforced with different

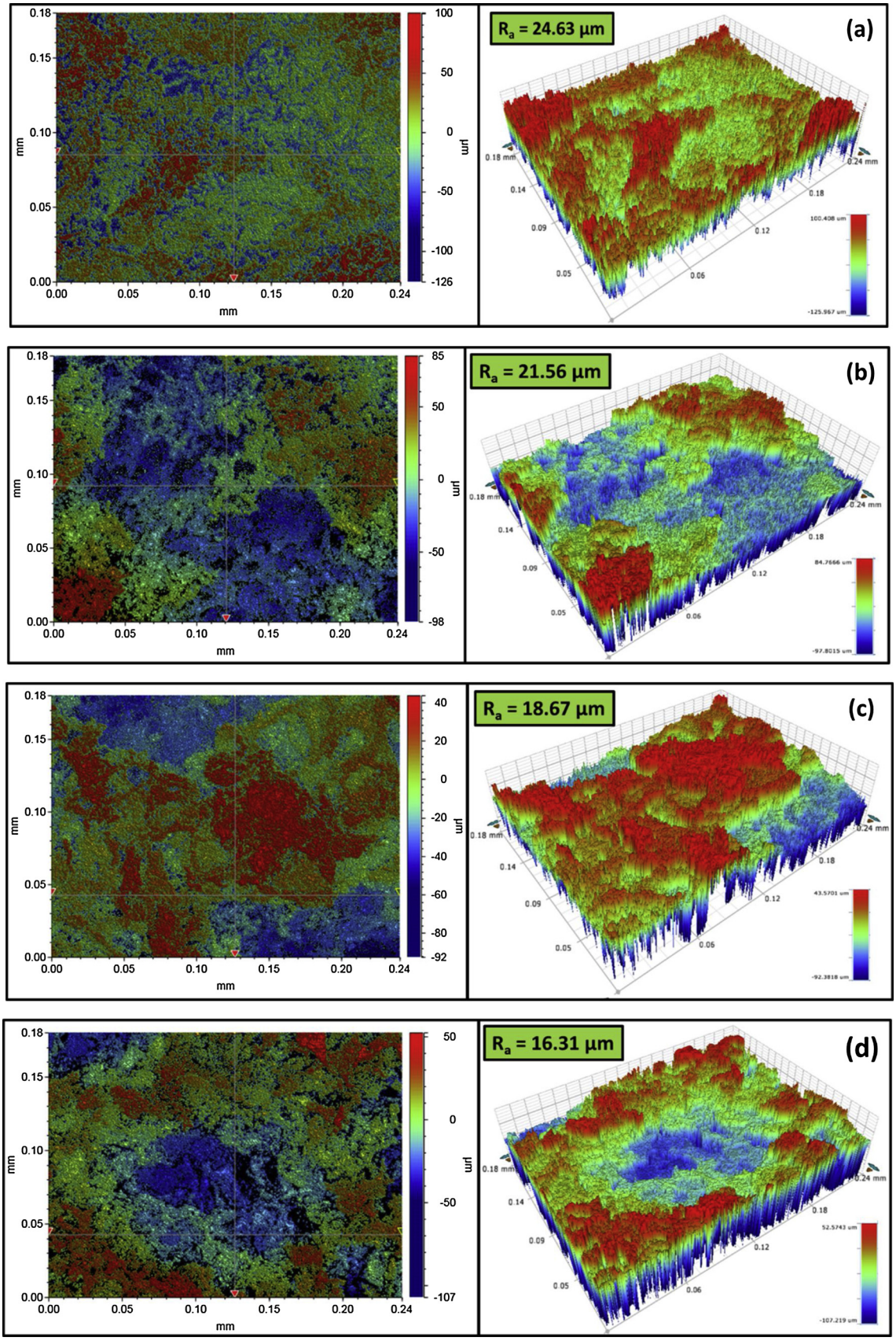

Fig. 11. 3D topographies and surface roughness values of the (a) AZXY9120 alloy; (b) NC1, (c) NC2, and (d) NC3 nanocomposites after removal of the corrosion products.

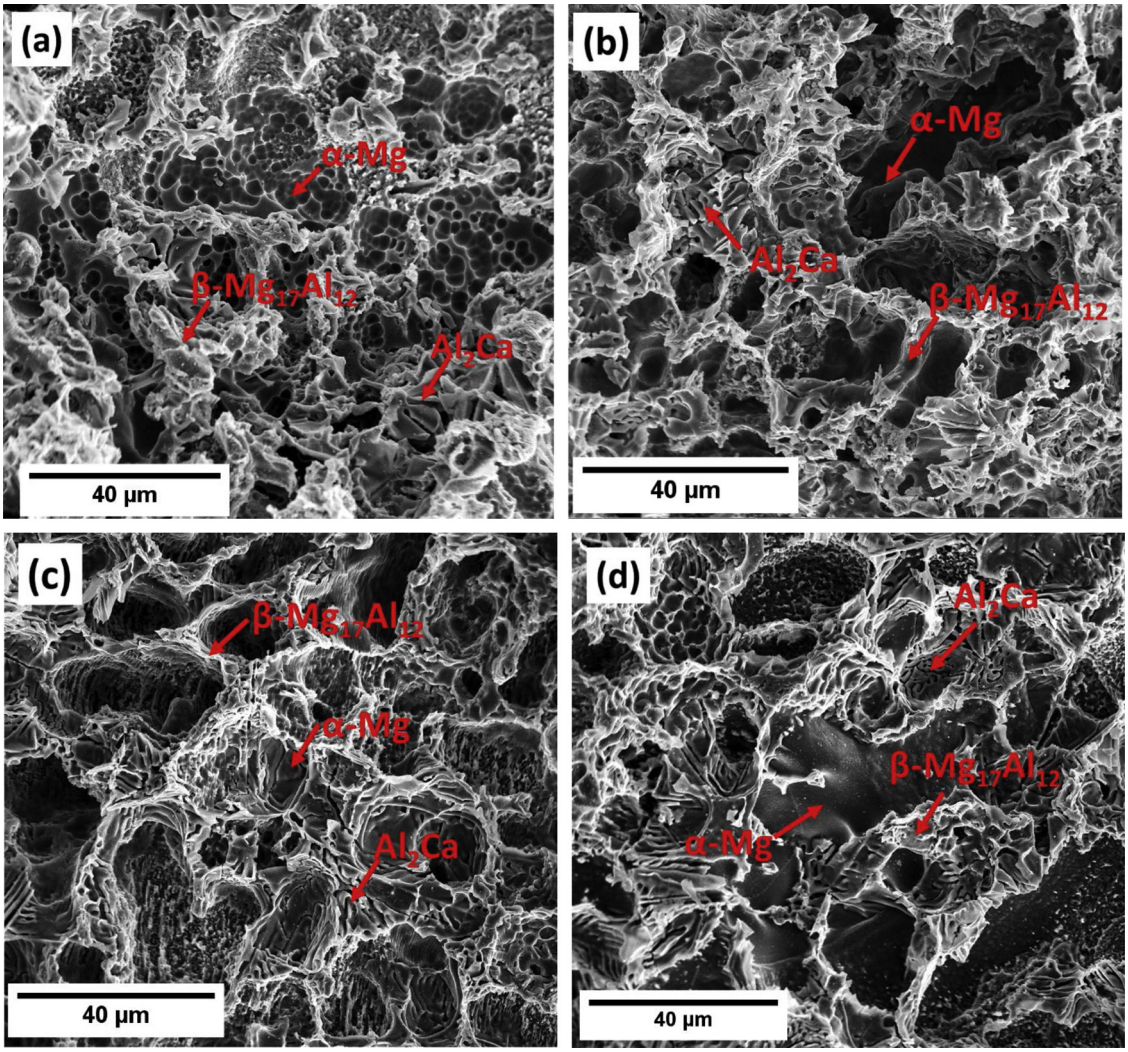

Fig. 12. SEM micrographs of the corroded surfaces of the (a) AZXY9120 alloy; (b) NC1, (c) NC2, and (d) NC3 nanocomposites after removal of corrosion products.

weight percentages of SiC nanoparticles in 0.1 M NaCl solution. The major conclusions arising from this work are:

i The Volta potential measurement concluded that the β-$Mg_{17}Al_{12}$ phase is nobler than the Al_2Ca phase. The SiC nanoparticles additions in the AZ91 + 2.0Ca + 0.3Sb (wt.%)) alloy reduced the Volta potential of the β-$Mg_{17}Al_{12}$ phase present in the nanocomposites, and the reduction was 14% in the NC3 nanocomposite compared to the alloy.

ii All the nanocomposites demonstrated the lower weight-loss and lower volume of hydrogen evolution compared to the alloy. The corrosion rate of the NC3 nanocomposite was the lowest among the nanocomposites employed.

iii The SiC nanoparticles additions in the alloy shifted the open circuit potential to more noble values. All the nanocomposites displayed the lower corrosion current densities and lower corrosion rates than the alloy. Among the nanocomposites, the NC3 revealed the highest corrosion resistance.

iv The major corrosion products formed on the surfaces of the alloy and nanocomposites were $Mg(OH)_2$ and $MgCO_3$. The amount of corrosion products in the nanocomposites was lower than that in the alloy.

v The improved corrosion performance of the nanocomposites was attributed to the decrease in the potential difference between the α-Mg and β-$Mg_{17}Al_{12}$ phases, reduced quantity of the β-$Mg_{17}Al_{12}$ phase, and an increased amount of the Al_2Ca phase following the SiC nanoparticles additions.

Data availability

The raw/processed data required to reproduce these findings cannot be shared at this time as the data also forms part of an ongoing study.

Declaration of Competing Interest

The authors declare that they have no known competing financial interests or personal relationships that could have appeared to influence the work reported in this paper.

Acknowledgment

This research was financially supported by the Council of Scientific and Industrial Research (CSIR), New Delhi, India through the Scheme No.: 22(626)/13-EMR-II, dated: 26-02-2013. The authors gratefully acknowledge the use of corrosion testing equipment obtained from the funding of Council of Scientific & Industrial Research, India through the Scheme No.: (0755)/17/EMR-II.

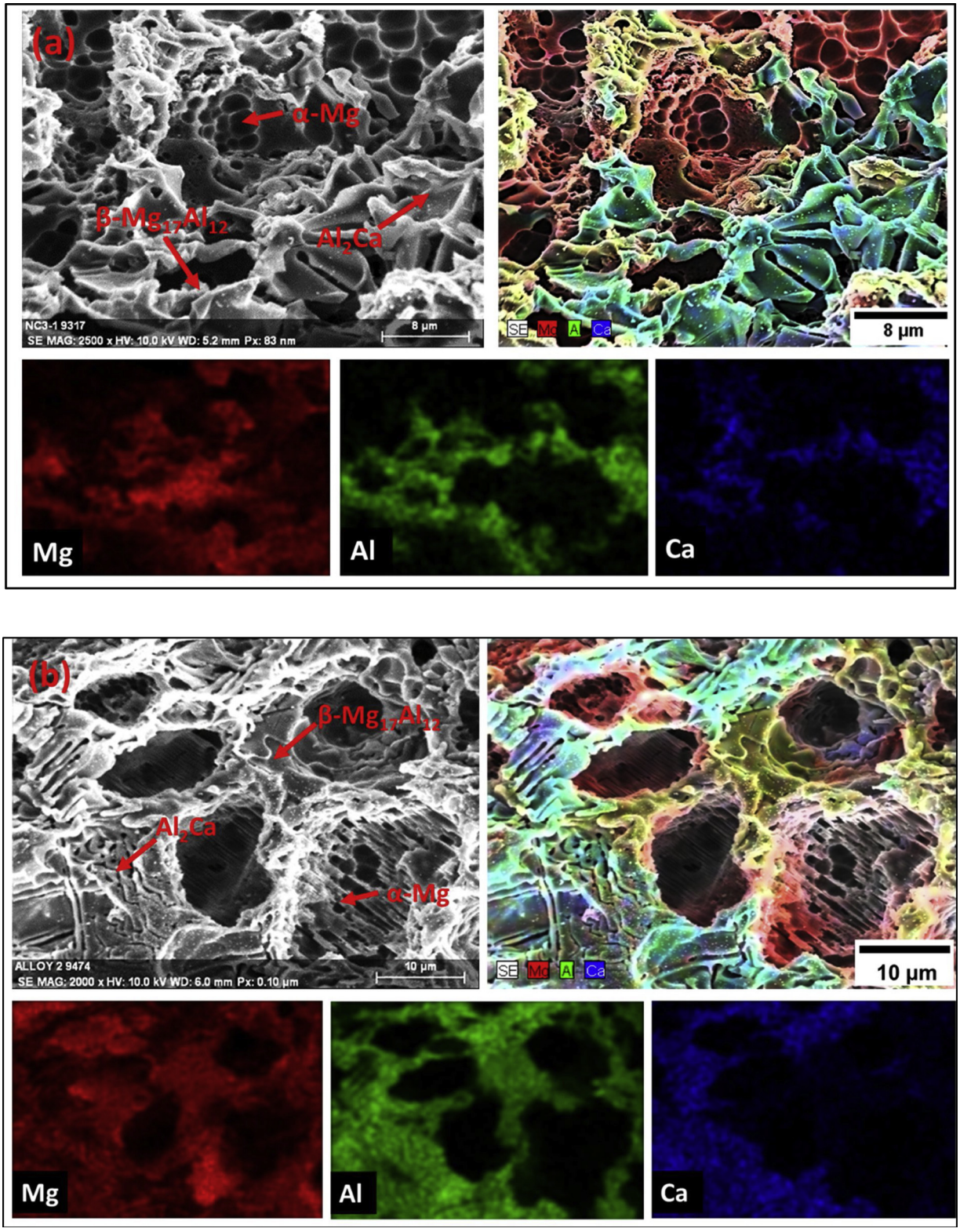

Fig. 13. SEM elemental mappings taken from the (a) AZXY9120 alloy, and (b) NC3 nanocomposite after removal of the corrosion products.

Appendix A. Supplementary data

Supplementary material related to this article can be found, in the online version, at doi:https://doi.org/10.1016/j.corsci.2020.108444.

References

[1] B.L. Mordike, T. Ebert, Magnesium Properties - applications - potential, Mater. Sci. Eng. A 302 (2001) 37–45, https://doi.org/10.1016/S0921-5093(00)01351-4.
[2] G. Song, A. Atrens, Corrosion mechanisms of magnesium alloys, Adv. Eng. Mater. 1 (1999) 11–33, https://doi.org/10.1002/(SICI)1527-2648(199909)1.
[3] A.A. Luo, M.O. Pekguleryuz, Cast magnesium alloys for elevated temperature applications, J. Mater. Sci. 29 (1999) 5259–5271, https://doi.org/10.1007/

BF01171534.
[4] A.A. Luo, Recent magnesium alloy development for elevated temperature applications, Int. Mater. Rev. 49 (2004) 13–30, https://doi.org/10.1179/095066004225010497.
[5] T. Zhang, Y. Li, F. Wang, Roles of β phase in the corrosion process of AZ91D magnesium alloy, Corros. Sci. 48 (2006) 1249–1264, https://doi.org/10.1016/j.corsci.2005.05.011.
[6] B.C. Pai, U.T.S. Pillai, P. Manikandan, A. Srinivasan, Modification of AZ91 Mg alloys for high temperature applications, Trans. Indian Inst. Met. 65 (2012) 601–606, https://doi.org/10.1007/s12666-012-0166-1.
[7] K. Gusieva, C.H.J. Davies, J.R. Scully, N. Birbilis, Corrosion of magnesium alloys: the role of alloying, Int. Mater. Rev. 60 (2015) 169–194, https://doi.org/10.1179/1743280414Y.0000000046.
[8] M. Grimm, A. Lohmuller, R.F. Singer, S. Virtanen, Influence of the microstructure on the corrosion behaviour of cast Mg-Al alloys, Corros. Sci. 15 (2019) 195–208, https://doi.org/10.1016/j.corsci.2019.04.024.
[9] H. Feng, S. Liu, Y. Du, T. Lei, R. Zeng, T. Yuan, Effect of second phases on the corrosion behavior of magnesium alloys, J. Alloys. Compd. 695 (2017) 2330–2338, https://doi.org/10.4028/www.scientific.net/msf.419-422.857.
[10] A.K.S. Bankoti, A.K. Mondal, C.S. Perugu, B.C. Ray, S. Kumar, Correlation of microstructure and electrochemical corrosion behavior of squeeze-cast Ca and Sb added AZ91 Mg alloys, Metall. Mater. Trans. A 48A (2017) 5106–5121, https://doi.org/10.1007/s11661-017-4244-1.
[11] H.Z. Ye, X.Y. Liu, Review of recent studies in magnesium matrix composites, J. Mater. Sci. 9 (2004) 6153–6171, https://doi.org/10.1023/B:JMSC.0000043583.47148.31.
[12] W.A. Ferrando, Review of corrosion and corrosion control of magnesium alloys and composite, J. Mater. Eng. 11 (1989) 299–313, https://doi.org/10.1007/BF02834140.
[13] W.M. Chan, F.T. Cheng, L.K. Leung, R.J. Horylev, T.M. Yue, Corrosion behavior of magnesium alloy AZ91 and its MMC in NaCl solution, Corros. Rev. 16 (1998) 43–52, https://doi.org/10.1515/CORRREV.1998.16.1-2.43.
[14] S. Tiwari, R. Balasubramaniam, M. Gupta, Corrosion behavior of SiC reinforced magnesium composites, Corros. Sci. 49 (2007) 711–725, https://doi.org/10.1016/j.corsci.2006.05.047.
[15] A. Pardo, S. Merino, M.C. Merino, I. Barroso, M. Mohedano, R. Arrabal, F. Viejo, Corrosion behaviour of silicon carbide particle reinforced AZ92 magnesium alloy, Corros. Sci. 51 (2009) 841–849, https://doi.org/10.1016/j.corsci.2009.01.024.
[16] M. Esmaily, N. Mortazavi, J.E. Svensson, M. Halvarsson, A.E.W. Jarfors, On the microstructure and corrosion behavior of AZ91/SiC composites produced by rheocasting, Mater. Chem. Phys. 180 (2016) 29–37, https://doi.org/10.1016/j.matchemphys.2016.05.016.
[17] C. Zhang, T. Zhang, Y. Wang, F. Wei, Y. Shao, G. Meng, F. Wang, K. Wu, Effect of SiC particulates on the corrosion behavior of extruded AZ91/SiC_p composites during the early stage of exposure, J. Electrochem. Soc. 162 (2015) C754–C766, https://doi.org/10.1149/2.0631514jes.
[18] B. Mingo, R. Arrabal, M. Mohedano, A. Pardo, E. Matykina, Corrosion and wear of PEO coated AZ91/SiC composites, Surf. Coat. Technol. 309 (2017) 1023–1032, https://doi.org/10.1016/j.surfcoat.2016.10.041.
[19] L.H. Hihara, P.K. Kondepudi, Galvanic corrosion between SiC monofilamaent and magnesium in NaCl, Na_2SO_4 and $NaNO_3$ solutions for application to metal-matrix composites, Corros. Sci. 36 (1994) 1585–1595, https://doi.org/10.1016/0010-938X(94)90055-8.
[20] C.A. Nunez-Lopez, H. Habazaki, P. Skeldon, G.E. Thompson, H. Karimzadeh, P. Lyon, T.E. Wilks, An investigation of microgalvanic corrosion using a model magnesium-silicon carbide metal matrix composite, Corros. Sci. 38 (1996) 1721–1729, https://doi.org/10.1016/S0010-938X(96)00068-6.
[21] F. Zucchi, G. Trabanelli, V. Grassi, A. Frignani, Corrosion behavior in sodium sulfate and sodium chloride solutions of SiC_p reinforced magnesium alloy metal matrix composites, Corrosion (2004) 362–368, https://doi.org/10.5006/1.3287744.
[22] A.K. Mondal, C. Blawert, S. Kumar, Corrosion behaviour of creep-resistant AE42 magnesium alloy-based hybrid composites developed for powertrain applications, Mater. Corros. (2015) 1150–1158, https://doi.org/10.1002/maco.201408071.
[23] M. Gupta, W.L.E. Wong, Magnesium-based nanocomposites: lightweight materials of the future, Mater. Charact. 105 (2015) 30–46, https://doi.org/10.1016/j.matchar.2015.04.015.
[24] M. Kukreja, R. Balasubramaniam, Q.B. Nguyen, M. Gupta, Enhancing corrosion resistance of Mg alloy AZ31B in NaCl solution using alumina reinforcement at nanolength scale, Corros. Eng. Sci. Technol. 44 (2009) 381–384, https://doi.org/10.1179/147842208X356857.
[25] H. Fukuda, J.A. Szpunar, K. Kondoh, R. Chromik, The influence of carbon nanotubes on the corrosion behaviour of AZ31B magnesium alloy, Corros. Sci. 52 (2010) 3917–3923, https://doi.org/10.1016/j.corsci.2010.08.009.
[26] M.C. Turhan, Q. Li, H. Jha, R.F. Singer, S. Virtanen, Corrosion behaviour of multiwall carbon nanotube/magnesium composites in 3.5% NaCl, Electrochim. Acta 56 (2011) 7141–7148, https://doi.org/10.1016/j.electacta.2011.05.082.
[27] K. Funatsu, H. Fukuda, R. Takei, J. Umeda, K. Kondoh, Quantitative evaluation of initial galvanic corrosion behavior of CNTs reinforced Mg–Al alloy, Adv. Powder Technol. 24 (2013) 833–837, https://doi.org/10.1016/j.apt.2013.02.002.
[28] M. Rashad, F. Pan, M. Asif, X. Chen, Corrosion behavior of magnesium-graphene composites in sodium chloride solutions, J. Magnes. Alloy. 5 (2017) 271–276, https://doi.org/10.1016/j.jma.2017.06.003.
[29] H. Dieringa, Properties of magnesium alloys reinforced with nanoparticles and carbon nanotubes: a review, J. Mater. Sci. 46 (2011) 289–306, https://doi.org/10.1007/s10853-010-5010-6.
[30] S. Ganguly, A.K. Mondal, Influence of SiC nanoparticles addition on microstructure and creep behavior of squeeze-cast AZ91-Ca-Sb magnesium alloy, Mater. Sci. Eng. A 718 (2018) 377–389, https://doi.org/10.1016/j.msea.2018.01.131.
[31] S. Ganguly, S. Sarkar, M. Masanta, A.K. Mondal, Effect of SiC nanoparticles on the wear behaviour of squeeze-cast AZ91–2.0Ca–0.3Sb alloy, Mater. Sci. Technol. 35 (2019) 1678–1689, https://doi.org/10.1080/02670836.2019.1639384.
[32] R.K.S. Raman, The role of microstructure in localized corrosion of magnesium alloys, Metall. Mater. Trans. A 35 (2004) 2525–2531, https://doi.org/10.1007/s11661-006-0233-5.
[33] B.N. Popov, Corrosion Engineering Principles and Solved Problems, Elseivier, 2015.
[34] G. Song, A. Atrens, D. StJohn, An hydrogen evolution method for the estimation of the corrosion rate of magnesium alloys, in: John Hryn (Ed.), Magnes. Technol. TMS, LA, 2001, pp. 255–262.
[35] Z. Shi, M. Liu, A. Atrens, Measurement of the corrosion rate of magnesium alloys using Tafel extrapolation, Corros. Sci. 52 (2010) 579–588, https://doi.org/10.1016/j.corsci.2009.10.016.
[36] K.B. Nie, X.J. Wang, K. Wu, X.S. Hu, M.Y. Zheng, Development of SiC_p/AZ91 magnesium matrix nanocomposites using ultrasonic vibration, Mater. Sci. Eng. A 540 (2012) 123–129, https://doi.org/10.1016/j.msea.2012.01.112.
[37] D.B. Blucher, J. Svensson, L. Johansson, M. Rohwerder, Scanning kelvin probe force microscopy a useful tool for studying atmospheric corrosion of MgAl alloys in situ, J. Electrochem. Soc. 151 (2004) B621–B626, https://doi.org/10.1149/1.1809590.
[38] B. Mingo, R. Arrabal, M. Mohedano, C.L. Mendis, R. Olmo, E. Matykina, N. Hort, M.C. Merino, A. Pardo, Corrosion of Mg-9Al alloy with minor alloying elements (Mn, Nd, Ca, Y and Sn), Mater. Des. 130 (2017) 48–58, https://doi.org/10.1016/j.matdes.2017.05.048.
[39] R. Arrabal, E. Matykina, A. Pardo, M.C. Merino, K. Paucar, M. Mohedano, P. Casajús, Corrosion behaviour of AZ91D and AM50 magnesium alloys with Nd and Gd additions in humid environments, Corros. Sci. 55 (2012) 351–362, https://doi.org/10.1016/j.corsci.2011.10.038.
[40] M. Mohedano, R. Arrabal, A. Pardo, M.C. Merino, K. Paucar, P. Casaju, E. Matykina, Salt spray corrosion behaviour of new Mg-Al alloys containing Nd or Gd, Corros. Eng. Sci. Technol. 48 (2013) 183–194, https://doi.org/10.1179/1743278212Y.0000000058.
[41] R. Jia, M. Zhang, L. Zhang, W. Zhang, F. Guo, Correlative change of corrosion behavior with the microstructure of AZ91 Mg alloy modified with Y additions, J. Alloys. Compd. 634 (2015) 263–271, https://doi.org/10.1016/j.jallcom.2015.02.019.
[42] C. Örnek, C. Leygraf, J. Pan, On the Volta potential measured by SKPFM– fundamental and practical aspects with relevance to corrosion science, Corros. Eng. Sci. Technol. 54 (2019) 185–198, https://doi.org/10.1080/1478422X.2019.1583436.
[43] G. Song, A. Atrens, Understanding magnesium corrosion a framework for improved alloy performance, Adv. Eng. Mater. 5 (2003) 837–858, https://doi.org/10.1002/adem.200310405.
[44] G.S. Frankel, A. Samaniego, N. Birbilis, Evolution of hydrogen at dissolving magnesium surfaces, Corros. Sci. 70 (2013) 104–111, https://doi.org/10.1016/j.corsci.2013.01.017.
[45] M. Esmaily, J.E. Svensson, S. Fajardo, N. Birbilis, G.S. Frankel, S. Virtanen, R. Arrabal, S. Thomas, L.G. Johansson, Fundamentals and advances in magnesium alloy corrosion, Prog. Mater. Sci. 89 (2017) 92–193, https://doi.org/10.1016/j.pmatsci.2017.04.011.
[46] M. Jönsson, D. Persson, D. Thierry, Corrosion product formation during NaCl induced atmospheric corrosion of magnesium alloy AZ91D, Corros. Sci. 49 (2007) 1540–1558, https://doi.org/10.1016/j.corsci.2006.08.004.
[47] S. Feliu Jr., A. Pardo, M.C. Merino, A.E. Coy, F. Viejo, R. Arrabal, Correlation between the surface chemistry and the atmospheric corrosion of AZ31, AZ80 and AZ91D magnesium alloys, Appl. Surf. Sci. 255 (2009) 4102–4108, https://doi.org/10.1016/j.apsusc.2008.10.095.
[48] S. Feliu Jr., I. Llorente, Corrosion product layers on magnesium alloys AZ31 and AZ61: Surface chemistry and protective ability, Appl. Surf. Sci. 347 (2015) 736–746, https://doi.org/10.1016/j.apsusc.2015.04.189.
[49] R. Walter, M. Bobby Kannan, Influence of surface roughness on the corrosion behaviour of magnesium alloy, Mater. Des. 32 (2011) 2350–2354, https://doi.org/10.1016/j.matdes.2010.12.016.
[50] R.B. Alvarez, H.J. Martin, M.F. Horstemeyer, M.Q. Chandler, N. Williams, P.T. Wang, A. Ruiz, Corrosion relationships as a function of time and surface roughness on a structural AE44 magnesium alloy, Corros. Sci. 52 (2010) 1635–1648, https://doi.org/10.1016/j.corsci.2010.01.018.